



# Advances in $\text{CaCl}_2$ -Assisted Direct Reduction of Chromite Processing

David Carter , Jason P. Coumans , and Dogan Paktunc

## Abstract

The Direct Reduction of Chromite (DRC) process has the potential to reduce energy consumption and reduce Greenhouse Gas (GHG) emissions for ferrochrome production, as needed to produce stainless steel and other specialty alloys. In the DRC process, Fe and Cr oxides in chromite are reduced at temperatures below their latent heat of fusion which substantially lowers energy requirements, resulting in the production of  $\text{M}_7\text{C}_3$ -type ferrochrome. In the present work, induration by oxidative sintering, reductant size, and reduction temperature were investigated at the exploratory level to advance our understanding of the DRC process. Induration by oxidative sintering was notably found to slow reaction kinetics and delay metallization, whereas smaller reductant sizes accelerate reaction kinetics. The influence of temperature on reaction kinetics was investigated in several experiments, and an energy barrier identified which may justify a DRC processing temperature of 1320 °C. After an extended time at 1320 °C, the amount of Cr present in the spinel and slag as measured by microprobe analysis are less than 0.43 wt% Cr as  $\text{Cr}_2\text{O}_3$ , which confirms high degrees of Cr metallization.

## Keywords

Chromite · Ferrochrome · Direct Reduction

## 1 Introduction

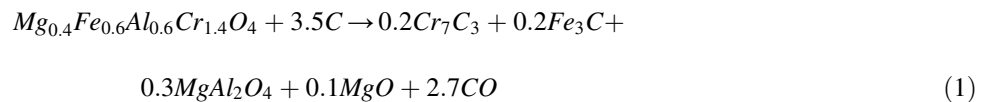
Chromium is an essential component of stainless steel, notably providing corrosion resistance, hardness, and toughness to the alloy. This makes stainless steel the material of choice for tubing, tanks, and many specialty alloy products. Global demand for chromium therefore increases with demand for stainless steel, which grew by 3.0% in industrialized countries, and 6.3% in developing and emerging countries between 2011 and 2017 [1]. In 2021, more than 58 million tonnes of stainless steel was produced globally [2]. The production methods for ferrochrome (FeCr), an alloy composed of iron, chromium, and carbon as needed to meet this stainless steel demand, are notably energy intensive and have a significant environmental impact. Energy requirements range from 2.4 to 4.8 MWh/t FeCr and GHG emissions can exceed 10.5 tCO<sub>2</sub>e/t FeCr, respectively [3–5]. The most energy intensive of these processes utilize DC Arc furnaces and Submerged Arc furnaces (SAF) which are responsible for producing more than 85% of the world's FeCr [6]. Less energy-intensive processing routes include the Outotec steel belt sintering process and the Glencore Premus process. These processes utilize CO off-gas from the downstream smelting furnace as a fuel to generate heat for preheating pelletized ore with binders and reductant particles on a steel belt or in a kiln prior to SAF smelting [7–10].

D. Carter (✉) · J. P. Coumans · D. Paktunc  
Natural Resources Canada, CanmetMINING, Ottawa, ON, Canada  
e-mail: [davidj.carter@nrcan-mcan.gc.ca](mailto:davidj.carter@nrcan-mcan.gc.ca)

As an alternative processing technology, Direct Reduction of Chromite (DRC), has been developed to improve resource utilization, competitiveness, and the need for value-added products in Canada [6, 11]. In the DRC process, which takes place at approximately 1300 °C, the energy required to overcome the high enthalpy of fusion for minerals with melting temperatures in excess of 1600 °C [12] is avoided. The limitations and advantages of the DRC process in comparison to conventional technologies have been published previously [4, 5, 13–15]. In this work, exploratory experiments have been conducted to advance DRC technology by investigating the effects of induration by oxidative sintering, reductant particle size, and temperature.

## 1.1 DRC Mechanism and Theory

In the DRC process, chromium ions are incongruently dissolved into a molten flux from chromite particles and transported to the surface of carbonaceous reductant particles where they are reduced [4]. The overall DRC reaction for a typical Ring of Fire (RoF) chromite composition is shown in Eq. 1. The Boudouard reaction, which relates to C transformation to CO by reacting with CO<sub>2</sub> gas, is shown in Eq. 2. Geometrically, the chromite dissolution and alloy (carbide) formation steps can be described by a shrinking core model [6]. Changes in the concentration of products with time are a function of reaction rate (function of temperature), reactant concentrations, and system geometry/rate-limiting mechanism (how physical characteristics vary) [17].



## 2 Materials and Methods

### 2.1 Materials

The reductant in this work is grade 4079 petroleum coke (PETcoke) with a minimum carbon content of 98% (determined by LOI) from Asbury Carbons (NJ, USA). Particle size ranges of PETcoke were prepared by rod milling followed by dry sieving to produce –75 μm, –106 + 75 μm, and –355 + 106 μm fractions. CaCl<sub>2</sub> (> = 97%) from Millipore-Sigma (Oakville, ON) was used as a flux based on the results of previous works investigating different fluxes [5]. The chromite ore comes from the Ring of Fire deposits in Northern Ontario, and is accompanied by minor Cr-bearing clinocllore, magnesite, and phlogopite as described previously [13]. The ore was concentrated by dry milling and sieving to a particle size range of –106 + 75 μm. This particle size range is the optimum determined in previous works [14]. XRF analysis of this ore is shown in Table 1.

### 2.2 Pelletization

Spherical pellets with a size of 12 ± 0.5 mm were pressed at a force of 1500 ± 100 N for 2 min with a manually operated hydraulic press. Each pellet contained chromite ore, PETcoke, and CaCl<sub>2</sub> as flux (O:R:F) with a ratio of 100:20–22:30 by mass. Water was added as a binder at a ratio of 6 wt% of the dry basemix to aid pelletization. Where indicated, pellets were rolled using water as needed with a Mars Mineral DP-14 pelletizer (Mars, PA).

**Table 1** Chemical composition of RoF chromite ore used in this study, based on X-Ray Fluorescence (XRF) analysis

	Al <sub>2</sub> O <sub>3</sub>	Cr <sub>2</sub> O <sub>3</sub>	Fe <sub>2</sub> O <sub>3</sub>	MgO	MnO	NiO	SiO <sub>2</sub>	TiO <sub>2</sub>	V <sub>2</sub> O <sub>5</sub>
Average [wt%]	12.78	44.54	20.29	13.66	0.19	0.17	5.32	0.34	0.17
Variability [wt%]	0.64	3.36	1.81	1.78	0.02	0.02	2.00	0.01	0.01

## 2.3 Thermal Processing

Pressed pellets were dried, and then reduced in a Deltech vertical tube furnace (Denver, CO), with Gr 5.0 Argon from Messer (Mississauga, ON) as a purge gas to maintain an inert atmosphere. 20 vol% CO<sub>2</sub> in N<sub>2</sub> was mixed using mass flow-controlled Gr 4.0 CO<sub>2</sub> and Gr 5.0 N<sub>2</sub> gases from Messer to produce an oxidizing atmosphere as needed. Four or 16 pellets were reduced simultaneously in each experiment as indicated. The furnace temperature is controlled using an alumina-sheathed R-type thermocouple inside the furnace cavity (external to the furnace tube); however, the temperature inside the tube better represents the temperature experienced by the pellets. The temperature inside the furnace tube was therefore measured at multiple temperatures using another alumina-sheathed R-type thermocouple, and these measured tube interior temperatures related to programmed furnace cavity temperatures. Thermal regimes shown in the figures describe the temperature experienced by pellets. Off-gas from reduction was cleaned using a gas conditioner, and then analyzed by a Siemens Ultramat-23 IR analyzer (Oakville, ON).

## 2.4 Characterization

X-Ray diffraction (XRD) analysis was conducted using a Rigaku D/MAX 2500 rotating-anode powder diffractometer with Cu K $\alpha$  radiation at 40 kV, 200 mA. Secondary (SE) and backscattered (BSE) electron images were acquired with a S-3200 N Hitachi microscope scanning electron microscope (SEM) operated at an accelerating voltage of 20 kV. Quantitative X-ray microanalyses by wavelength-dispersive spectrometry and some BSE images were obtained using a JEOL JXA 8230 electron probe X-ray microanalyzer (EPMA) at an accelerating voltage of 20 kV, 15–25 nA beam current, with a focused or diffuse beam up to 10 microns, depending on the area to be analyzed.

---

## 3 Results and Discussion

### 3.1 Influence of Induration by Oxidative Sintering

Research by others has found that induration by oxidatively sintering chromite ore-containing pellets at a temperature of approximately 1000 °C results in strength improvements and mineralogical transformations which can improve ferrochrome processing in arc furnaces [9, 10, 16–20]. In the Outotec process, which features this pretreatment step, a minimal amount of reductant is pelletized with chromite ore and a clay binder to form pellets which are heated in an oxidizing atmosphere for a short period of time on a steel sintering belt. During this step, pellet strength increases due to sintering of the fine clay and gangue mineral particles in the outer layer of each pellet. More reductant is then added with preheated pellets to a SAF to realize complete reduction of chromite. This process utilizes the oxidation of carbon to sinter pellets which increases the reducibility of chromite by increasing the effective surface area due to recrystallization of Fe<sub>3</sub>O<sub>4</sub> to Fe<sub>2</sub>O<sub>3</sub> [10]. It is hypothesized that a thin and minimally porous rim formed around DRC pellets by oxidative sintering will improve the rate of carbothermal reduction of chromite by likewise recrystallizing Fe<sub>3</sub>O<sub>4</sub> to Fe<sub>2</sub>O<sub>3</sub>, increasing CO partial pressure, and the ratio of CO/CO<sub>2</sub> during reduction.

To investigate the effect of oxidative sintering on reduction, pellets were exposed to an oxidizing atmosphere for a defined amount of time as described in section “[Thermal Processing](#)”, and the influence of duration and proportion of reductant particles relative to ore were varied. SE and BSE images of pellets that were oxidized and then reduced are shown in Figs. 1 and 3, respectively. CO flux and cumulative evolved CO as a function of time for relevant experiments are shown in Fig. 2.

Figure 1a, b show that most of the PETcoke particles are completely consumed in the outer rim due to oxidation by CO<sub>2</sub>, which can be distinguished from the pellet’s core. The darker rim of the pellet, as shown in Fig. 1, can be attributed to the formation of metal oxide particles during oxidation that are more easily polished away than neighboring particles. Figure 1c notably shows that the oxidized rim around the pellet is continuous, albeit not of a uniform thickness. A reduced proportion of ore:PETcoke (100:20 vs 100:22) did not significantly affect the rim’s thickness (approximately 700 ± 200 μm). The effects of these conditions on reduction following oxidative sintering are shown in the evolved CO gas data (Fig. 2) and BSE images of representative pellet grains (Fig. 3).

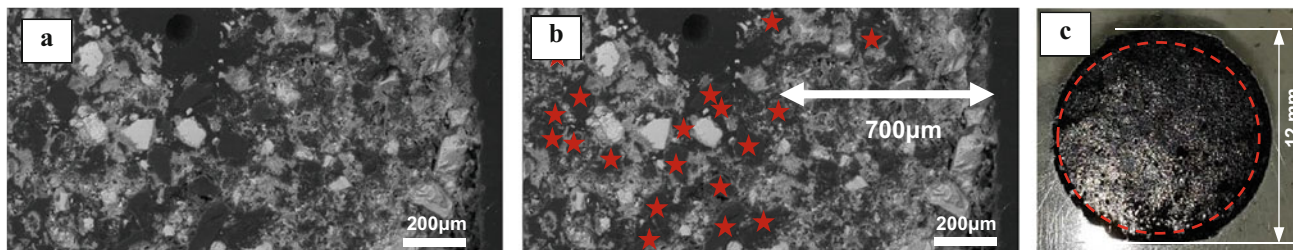


**Fig. 1** (a, b) Secondary electron images of the rim of a pellet containing 100:22:30 Ore:PETcoke:CaCl<sub>2</sub> that were oxidized at a programmed furnace temperature of 1000 °C for 10 min. PETcoke particle size is  $-106 + 75 \mu\text{m}$ . Stars denote PETcoke particles. (c) Flash photograph of the polished pellet cross section from Fig. a, b. Dashed line denotes approximate rim boundary.

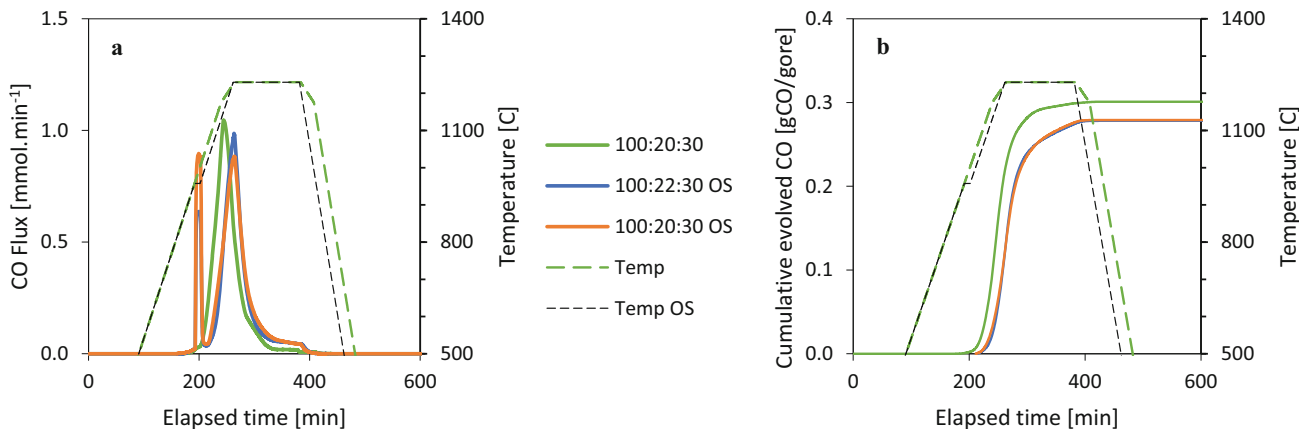


**Fig. 2** (a) Molar flux of CO evolved during induration and reduction of pellets with the indicated proportions of O:R:F shown as a function of time according to the thermal regimes shown. (b) Cumulative CO evolved during induration and reduction of pellets corresponding to Fig. a. Each experiment was conducted using 4 pellets and a purge gas flow rate of  $0.5 \text{ L}_{\text{AR}} \cdot \text{min}^{-1}$ . The temperatures shown have been calculated with a calibration curve to describe the temperature experienced by pellets inside the furnace tube based on the programmed furnace cavity temperature. Dwell time at the maximum temperature is 2 h. PETcoke particle size is  $-106 + 75 \mu\text{m}$ . OS denotes experiments including 10 min of oxidative sintering prior to reduction. 100:22:30 OS pellets were rolled. CO measured during induration does not represent FeCr metallization and has been excluded from Fig. b

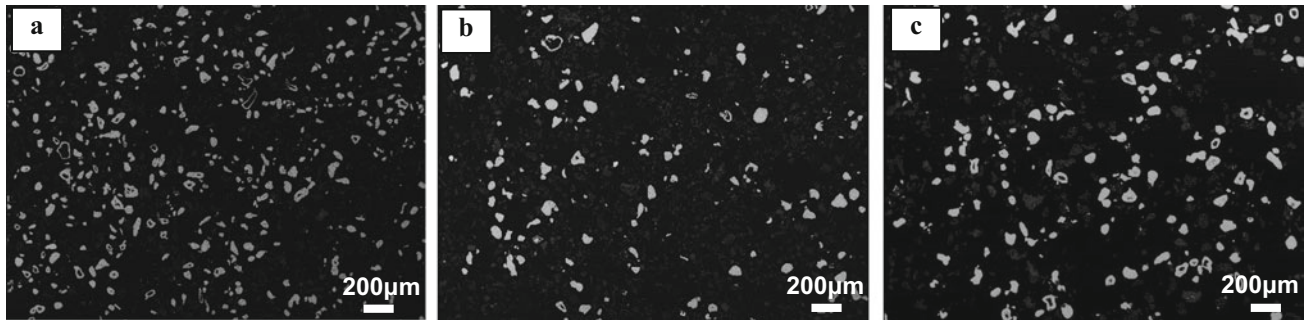
Figure 2a shows that the greatest CO flux, which represents the fastest reaction kinetics for reduction, was observed for pellets that were not oxidatively sintered. Of the reduction experiments conducted on oxidatively sintered pellets using different proportions of PETcoke, the CO flux profiles are comparable, suggesting similar kinetics. The greatest peak CO flux from these two oxidatively sintered and then reduced experiments is observed when a greater proportion of PETcoke is used.

Figure 2b shows that the most CO was evolved for non-indurated pellets, implying greater FeCr metallization than pellets that were indurated. This difference can be attributed to C from PETcoke reacting with CO<sub>2</sub> from the oxidizing atmosphere during oxidative sintering as described by the Boudouard reaction (Eq. 2), which reduced the available PETcoke for later metallization by carbothermal reduction.

Figure 3 shows representative BSE images of reduced pellet grains from the experiments whose CO flux profiles are shown in Fig. 2. The largest particles of FeCr with the least number of unreacted PETcoke cores are found in Fig. 3c, which represents the non-oxidatively sintered pellets. Of the pellets that were oxidatively sintered prior to reduction, the pellets containing a lower proportion of PETcoke in the charge contain less unreacted PETcoke (Fig. 3b).

### 3.2 Influence of Reductant Particle Size

The rate of metallization is a function of the reductant particle size and relationships between surface area and volume. In this way, the reductant particle size does not reduce the energetic requirement for Cr reduction to  $\text{M}_7\text{C}_3$ , rather, smaller reductant particles will accelerate reaction kinetics due to a greater surface area to volume ratio in comparison to larger reductant particles. Experiments were conducted using pellets containing PETcoke particles with the following size ranges:  $-75 \mu\text{m}$ ,  $-106 + 75 \mu\text{m}$ , and  $-355 + 106 \mu\text{m}$ . The resulting CO flux profiles are shown in Fig. 4.



**Fig. 3** Representative BSE images of grains from reduced pellets whose evolved CO gas data is shown in Fig. 2. (a) Pellets were rolled and composed of 100:22:30 O:R:F, oxidatively sintered for 10 min prior to reduction. (b) Pellets were composed of 100:20:30 O:R:F, oxidatively sintered for 10 min prior to reduction. (c) Pellets were composed of 100:20:30 O:R:F, reduced without oxidative sintering

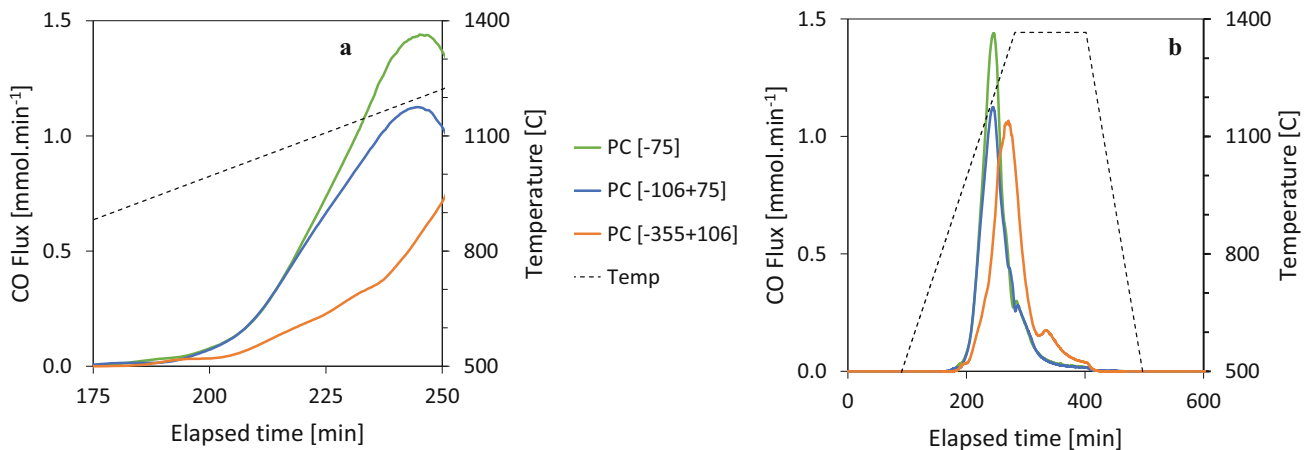


**Fig. 4** CO flux as a function of time subject to the thermal regime shown for pellets containing different size fractions of PETCoke as indicated. Each experiment was conducted using 4 pellets and a purge gas flow rate of  $0.5 \text{ L}_{\text{AR}} \cdot \text{min}^{-1}$ . The temperatures shown have been calculated with a calibration curve to describe the temperature experienced by pellets inside the furnace tube based on the programmed furnace cavity temperature. (a) Shows CO flux between 175 and 250 min, and has been taken from (b)

Figure 4a shows that at a temperature of approximately  $860 \text{ }^\circ\text{C}$ , CO production starts for all experiments due to the reduction of Fe, which is consistent with previous work [4, 14]. Figure 4a also shows that the initial rate and the integral area of the CO flux are inversely proportional to PETcoke size. Additionally, there is very little difference between the time and temperature of peak CO flux for  $-75 \text{ }\mu\text{m}$  and  $-106 + 75 \text{ }\mu\text{m}$  PETcoke. Unlike the  $-106 \text{ }\mu\text{m}$  PETcoke, the  $-355 + 106 \text{ }\mu\text{m}$  PETcoke experiments exhibit a delay of the maximum observed CO. Furthermore, Fig. 4b shows that CO flux does not return to the baseline during the later stages of reduction at isothermal conditions. Therefore, complete metallization has not been reached for any of the experiments; however, the order of increasing degrees of metallization based on PETcoke size is  $-75 \text{ }\mu\text{m}$ ,  $-106 + 75 \text{ }\mu\text{m}$ ,  $-355 + 106 \text{ }\mu\text{m}$ . These observations demonstrate that experiments with larger PETcoke sizes are slower than experiments with smaller PETcoke sizes. Smaller particles have a greater surface area to volume ratio in comparison to larger particles. Therefore, these experiments demonstrate the role of surface area as related to particle size on the reaction kinetics of the DRC process.

### 3.3 Influence of Temperature and Hold Time

To investigate the influence of temperature on the degree of metallization and kinetics of the DRC reaction, experiments were conducted at various temperatures, and their CO flux profiles are shown in Fig. 5. Representative residual phases and FeCr particles from the experiments whose CO flux profiles are shown in Fig. 5b were characterized by XRD (Fig. 6) and EPMA (Fig. 7; Tables 2 and 3).

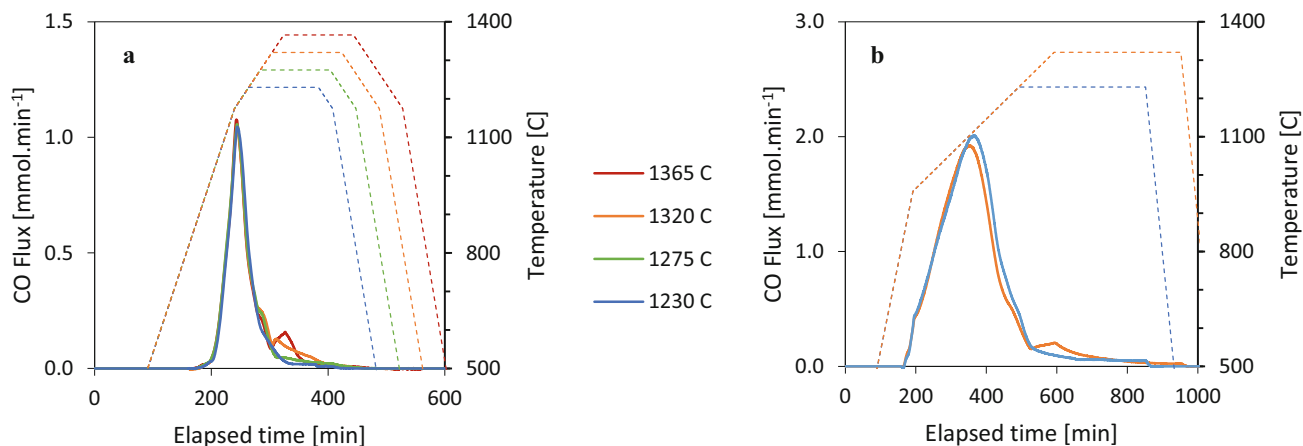


**Fig. 5** CO flux as a function of time subject to the thermal regimes with different isothermal temperatures as shown. The PETcoke size used for all pellets was  $-106 + 75 \mu\text{m}$ . The temperatures shown have been calculated with a calibration curve to describe the temperature experienced by pellets inside the furnace tube based on the programmed furnace cavity temperature. (a) Each experiment was conducted using 4 pellets and a purge gas flow rate of  $0.5 \text{ L}_{\text{AR}} \cdot \text{min}^{-1}$ . (b) Each experiment was conducted using 16 pellets and a purge gas flow rate of  $1.0 \text{ L}_{\text{AR}} \cdot \text{min}^{-1}$

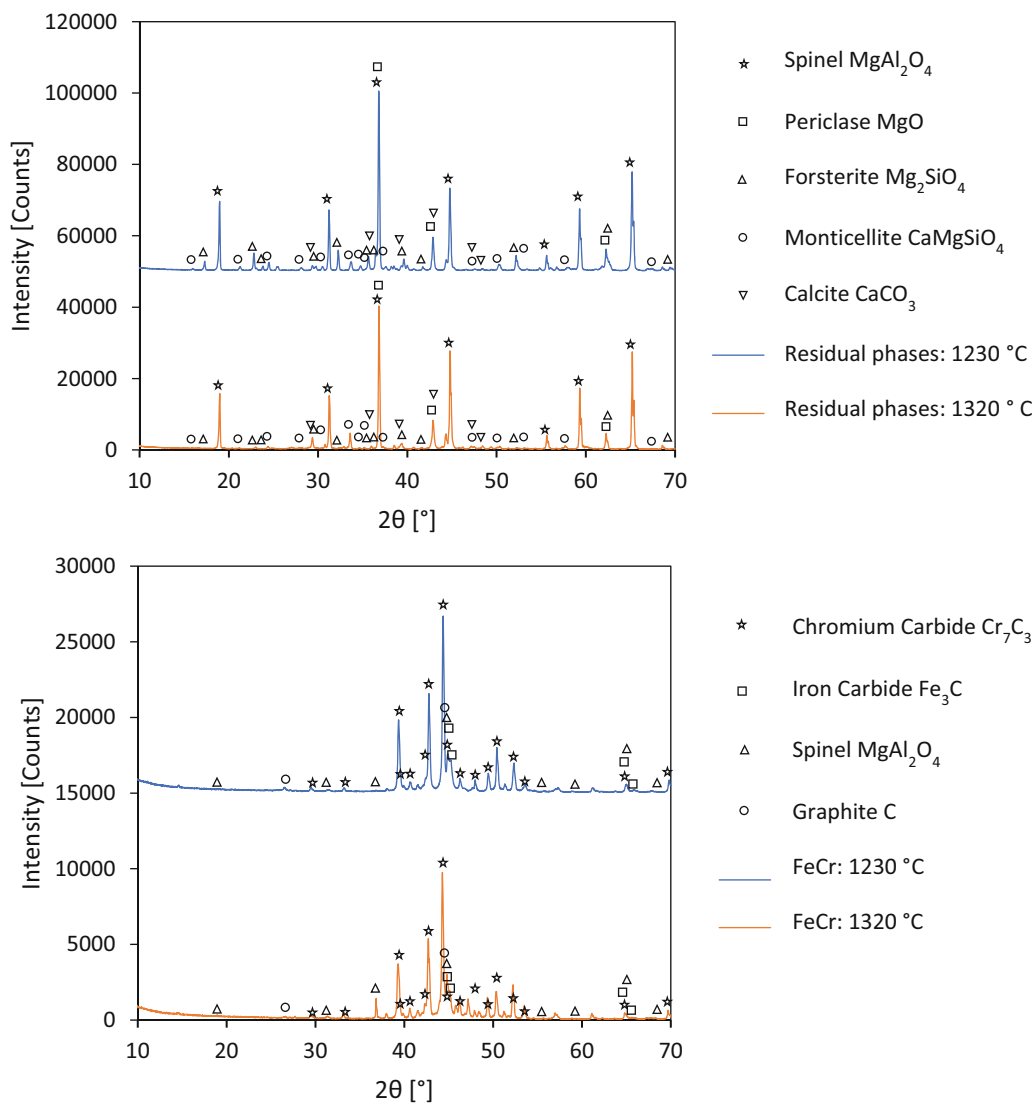


**Fig. 6** XRD analysis of residual phases (top) and FeCr (bottom) products that were reduced at an isothermal temperature of 1230 °C and 1320 °C as shown in Fig. 5b

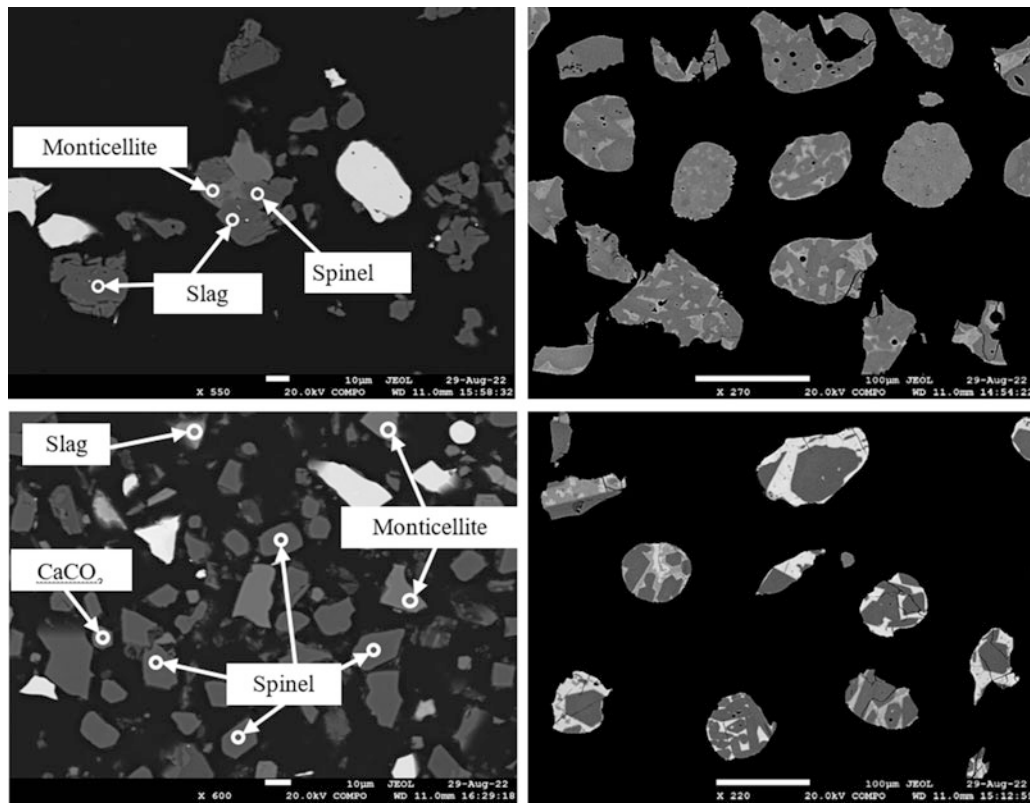


**Fig. 7** BSE images showing representative phases analyzed using microprobe. Residual phases (left) and FeCr (right) products that were reduced at an isothermal temperature of 1230 °C (top) and 1320 °C (bottom) as shown in Fig. 5b. Bright regions of FeCr particles are rich in Fe, whereas darker FeCr regions are richer in Cr

**Table 2** Composition of residual phases as determined by EPMA

T <sub>iso</sub> [°C]	Dominant phase	[wt%]						
		SiO <sub>2</sub>	MgO	Al <sub>2</sub> O <sub>3</sub>	Cr <sub>2</sub> O <sub>3</sub>	FeO	CaO	Cl
1320	Spinel (11)	b.d.l.	<b>31.14</b> [30.51–31.72]	<b>69.74</b>	<b>0.23</b> [0.14–0.43]	b.d.l.	b.d.l.	n.d.
	Slag (5)	<b>32.72</b> [29.81–36.50]	<b>7.65</b> [3.08–12.61]	<b>0.57</b> [0.05–2.29]	b.d.l.	b.d.l.	<b>54.5</b> [51.42–56.73]	<b>5.47</b> [0.01–9.19]
	Monticellite (5)	<b>37.82</b> [37.58–37.98]	<b>25.71</b> [25.64–25.91]	b.d.l.	b.d.l.	b.d.l.	<b>36.83</b> [36.49–37.30]	b.d.l.
1230	Spinel (11)	b.d.l.	<b>30.77</b> [30.53–31.00]	<b>68.67</b> [66.35–69.93]	<b>0.89</b> [0.05–2.61]	b.d.l.	b.d.l.	n.d.
	Forsterite (11)	<b>42.47</b> [41.91–43.50]	<b>56.99</b> [56.24–58.10]	b.d.l.	<b>1.10</b> [0.05–1.62]	b.d.l.	<b>0.81</b> [0.49–1.61]	b.d.l.
	Monticellite (7)	<b>38.37</b> [38.30–38.59]	<b>28.5</b> [27.41–29.67]	b.d.l.	b.d.l.	b.d.l.	<b>33.76</b> [32.50–34.99]	b.d.l.

Numbers in brackets next to the dominant phase species indicate the number of points that have been averaged. The  $\pm 3\sigma$  standard errors are as follows: 0.34 SiO<sub>2</sub>, 0.23 MgO, 0.42 Al<sub>2</sub>O<sub>3</sub>, 0.18 Cr<sub>2</sub>O<sub>3</sub>, 0.09 FeO, 0.18 CaO, 0.01 Cl. [] Denote the range of measured values when greater than 3 $\sigma$  standard error. n.d. and b.d.l. denote element/oxides that were not detected or below detection limits

Figures 5a, b show that the main CO flux peaks overlap within experimental datasets where the thermal profiles match, which demonstrates that the pellet compositions and physical attributes were well controlled. As shown in Fig. 5a, a noticeably greater amount of CO is generated by pellets that were held isothermally for 120 min at 1320 °C and 1365 °C in comparison to pellets that were held at 1230 °C and 1275 °C for 120 min. Figure 5b similarly demonstrates that experiments held at 1320 °C generate more CO than experiments at 1230 °C for the same isothermal duration which was 360 min. These results demonstrate the increased degree of metallization that can be reached since the isothermal temperatures the pellets

**Table 3** Composition (atomic %) of alloy concentrates from experiments whose CO flux profiles are shown in Fig. 5b, as determined by EPMA

	1320 °C				1230 °C			
	Fe	Cr	Si	C	Fe	Cr	Si	C
Alloy 1 (Cr-rich, low Si)	<b>12.7</b> [10.42–17.55]	<b>60.7</b> [56.46–62.90]	<b>b.d.l.</b>	<b>26.1</b> [25.46–27.06]	<b>18.1</b> [15.77–22.21]	<b>55.2</b> [50.57–57.47]	<b>b.d.l.</b>	<b>26.2</b> [24.27–27.66]
Alloy 2 (Cr-rich, with Si)	<b>34.1</b> [33.43–34.86]	<b>38.8</b> [38.35–39.28]	<b>14.5</b> [14.00–14.91]	<b>11.5</b> [11.27–11.69]	<b>15.0</b>	<b>47.3</b>	<b>15.1</b>	<b>21.5</b>
Alloy 3 (Fe-rich, with Si)	<b>52.1</b> [41.19–62.94]	<b>28.1</b> [16.06–36.60]	<b>17.3</b> [13.46–20.71]	<b>1.5</b> [0.00–8.80]	<b>58.0</b> [37.02–65.36]	<b>20.0</b> [11.48–36.01]	<b>18.5</b> [14.71–21.82]	<b>2.2</b> [0.00–11.07]

Compositions of Alloy 2 have been determined using 1 and 2 microprobe points for 1230 °C and 1320 °C, respectively. Other average compositions have been determined using 8–28 points. [] Denote the range of measured values. The  $\pm 3\sigma$  standard errors are 0.5 for Fe and Cr, and 0.02 for Si. C was determined by difference. b.d.l. denotes elements that were below detection limits.



experienced were maintained for the same duration. It was previously observed with XANES that Cr metallization from chromite can be increased from 58.6% at 1200 °C, to 100% at 1400 °C, and predicted using FACTSAGE software to be 86.7 wt%, 98.5 wt%, and 100 wt% at temperatures of 1200 °C, 1300 °C, and 1400 °C, respectively [6, 14].

The CO flux profiles in Fig. 5b are notably broader than in Fig. 5a due to the slower rate of heating during their thermal regime. Figure 5a, b also show a second increase in CO flux for experiments that were performed at 1320 °C and above, which is more discernible in Fig. 5b due to the slower ramp rate that has been used. As metallization proceeds and reductant is consumed, CO flux again decreases. The second CO flux peak is a result of changes to the reaction rate which are caused by an energy-related barrier being overcome. This energy-related barrier is most likely related to the diffusion of reactant and product species across alloy rims that become thicker as metallization proceeds and is the topic of a future study. With respect to the feasibility of the DRC process, Fig. 5 demonstrates that an operating temperature equal to or exceeding 1320 °C could be justified to overcome an energy-related barrier and increase Cr recovery instead of longer durations at lower temperatures.

The XRD profiles shown in Fig. 6 qualitatively show the mineralogical differences between the FeCr and residual phases resulting from the different isothermal temperatures that were experienced during the experiments whose CO flux profiles are shown in Fig. 5b. For both residual phase samples, MgAl<sub>2</sub>O<sub>4</sub> spinel and MgO dominate as described by Eq. 1. The residual-phase XRD profiles additionally show a slightly greater proportion of forsterite collected from reduction at an isothermal temperature of 1230 °C, and a slightly greater proportion of monticellite collected from reduction at an isothermal temperature of 1320 °C. The FeCr XRD profiles in Fig. 6 show that similar phases containing Fe and Cr are present in both alloy samples, with minor MgAl<sub>2</sub>O<sub>4</sub> from contamination. At a 2θ angle of 26.5°, a slightly greater amount of graphite can be seen for the FeCr collected from reduction at an isothermal temperature of 1230 °C, which can be attributed to excess carbon relative to the amount of reducible iron and chromium species at 1230 °C.

Figure 7 shows that at both investigated temperatures, the residual phase particles (which includes Cr-depleted spinel) are generally more angular than the FeCr particles. Phase identifications made by XRD (Fig. 6) are complemented by EPMA (Table 2). Additionally, the EPMA results demonstrate that low amounts of Cr measured as Cr<sub>2</sub>O<sub>3</sub> are present in the spinel particles of both experiments. The samples from reduction at 1320 °C exhibited the lowest Cr concentrations in the spinel with an average value of 0.23 wt% Cr measured as Cr<sub>2</sub>O<sub>3</sub>, as expected from the high degree of metallization based on FACTSAGE predictions. This finding demonstrates that a significant amount of Cr can be recovered from chromite as FeCr at a temperature of 1320 °C. Furthermore, the CO profiles in Fig. 5b show that more than 4 h at 1320 °C is required for the CO flux to stop, indicating a high degree of reduction consistent with Cr in spinel.

The EPMA analyses shown in Table 2 additionally indicates that the slag from reduction at 1320 °C contains a wide range of Cl concentrations. As Cl containing phases were not identified in the XRD profile shown in Fig. 6, the measured Cl from reduction at 1320 °C was present in an amorphous slag phase. Similarly, a range of Ca-Si-Mg slag compositions, as determined by EPMA, were identified from reduction at 1320 °C, which likewise suggest their presence in an amorphous phase. Consistent with the XRD results, EPMA characterization confirmed that particles with compositions characteristic of monticellite could be identified in both 1230 and 1320 °C slag products, whereas forsterite could only be analyzed in the 1230 °C slag.

The BSE images from Fig. 7 reveal that the FeCr particles are composed of multiple alloy phases. The FeCr alloy EPMA results in Table 3 notably show that Si can be abundant, which is unexpected at temperatures of 1230 °C according to the Ellingham diagram for carbothermic reduction of SiO<sub>2</sub> [21]. Additional evidence is required to describe a mechanism for silicon reduction during DRC, which is currently under investigation by the authors.

---

## 4 Conclusion

In this work, exploratory experiments have been conducted to investigate the impacts of induration by oxidative sintering, PETcoke particle size, and temperature on advancing DRC technology. Induration by oxidative sintering was found to produce mineralogical changes in DRC pellets as well as a continuous partially porous rim. However, pellets that were indurated in this way did not demonstrate accelerated reaction kinetics. The additional complexity of oxidative sintering to the DRC process therefore does not seem to be justified based on the exploratory experiments carried out in this work. Reducing PETcoke size was observed to accelerate reduction kinetics through greater availability of reductant surface area for metallization. This finding shows that reductant particle size can be reduced in the DRC process to minimize waste due to over-grinding and maximize pellet throughput. At the same time, it must be considered that smaller FeCr particles are more difficult to separate from similarly sized slag and spinel particles and so the processing requirements of product liberation should be considered in future research. Reaction kinetics as a function of isothermal temperature following ramped pellet

heating was also investigated, and an energy barrier that can be overcome with a modest increase in temperature to realize faster and greater Cr recovery from chromite was identified. Finally, experiments were conducted over an extended time at temperatures of 1320 °C and 1230 °C, which are above and below the previously identified energy barrier. The run products from these experiments were characterized using EPMA and XRD which show the mineralogical changes that take place as the temperature is increased. These changes include a greater proportion of monticellite in the residual phase mineralogy, distinguishable exsolved alloy phases, and the presence of Si in FeCr.

**Acknowledgments** This project has been funded by CanmetMINING, Natural Resources Canada, under the Critical Minerals Research, Development and Demonstration program. The authors would also like to thank Bhavya Bhatt and Chloe Castell for their assistance in conducting reduction experiments, as well as Derek Smith, and Dominique Duguay for their analyzing samples using XRD and Microprobe, respectively.

## References

1. Pariser HH, Backeberg NR, Masson OCM, Bedder JCM (2018) Changing nickel and chromium stainless steel markets. Proc 15th Int Ferro-Alloys Congr INFACON 2018 118:1–12. <https://doi.org/10.17159/2411-9717/2018/v118n6a1>
2. World Stainless. <https://www.worldstainless.org/statistics/stainless-steel-meltshop-production/stainless-steel-meltshop-production-2015-2021>. Last accessed 21 Apr 2023
3. Johnson J, Reck BK, Wang T, Graedel TE (2008) The energy benefit of stainless steel recycling. Energy Policy 36:181–192. <https://doi.org/10.1016/j.enpol.2007.08.028>
4. Yu D, Paktunc D (2018) Calcium chloride-assisted segregation reduction of chromite: Influence of reductant type and the mechanism. Fortschr Mineral 8(2):45–63. <https://doi.org/10.3390/min8020045>
5. Paktunc D, Thibault Y, Sokhanvaran S, Yu D (2018) Influences of alkali fluxes on direct reduction of chromite for ferrochrome production. J South African Inst Min Metall 118:1305–1314. <https://doi.org/10.17159/2411-9717/2018/v118n12a9>
6. Paktunc D (2021) Direct reduction of chromite – conceptual approach and overview. Technical report, CanmetMINING
7. Hamuyuni J, Johto H, Bunjaku A, Vatanen S, Pajula T, Mäkelä P, Lindgren M (2021) Simulation-based life cycle assessment of ferrochrome smelting technologies to determine environmental impacts. J Clean Prod 295:126503–126513. <https://doi.org/10.1016/j.jclepro.2021.126503>
8. Naiker O (2007) The development and advantages of XStrata's PREMUS process. Proc. 11th Int. Ferro-Alloys Congr. INFACON 2007 112–119. [http://refhub.elsevier.com/S2666-7908\(21\)00346-3/sref28](http://refhub.elsevier.com/S2666-7908(21)00346-3/sref28)
9. Gasik M (2013) Handbook of ferroalloys: theory and technology. Butterworth-Heinemann, Oxford
10. Kleynhans ELJ, Neizel BW, Beukes JP, Van Zyl PG (2016) Utilisation of pre-oxidised ore in the pelletised chromite pre-reduction process. Miner Eng 92:114–124. <https://doi.org/10.1016/j.mineng.2016.03.005>
11. Paktunc D (2022) Chromite R&D Initiative – Background, Objectives, Approach and Summary of Accomplishments. Technical report, CanmetMINING
12. Hockaday SAC, Bisaka K (2010) Some aspects of the production of ferrochrome alloys in pilot dc arc furnaces at mintek. Proc. 12th Int. Ferroalloys Congr. 367–376
13. Yu D, Paktunc D (2018) Kinetics and mechanisms of the carbothermic reduction of chromite in the presence of nickel. J Therm Anal Calorim 132:143–154. <https://doi.org/10.1007/s10973-017-6936-6>
14. Yu D, Paktunc D (2018) Direct production of ferrochrome by segregation reduction of chromite in the presence of calcium chloride. Metals 8(1): 69–85. <https://doi.org/10.3390/met8010069>
15. Sokhanvaran S, Paktunc D (2019) Method of direct reduction of chromite with cryolite additive. U.S. Patent No. 10,358,693
16. Glastonbury RI, Beukes JP, Van Zyl PG, Sadiki LN, Jordaan A, Campbell QP, Stewart HM, Dawson NF (2015) Comparison of physical properties of oxidative sintered pellets produced with UG2 or metallurgical grade South African chromite: a case study. J South African Inst Min Metall 115:699–706. <https://doi.org/10.17159/2411-9717/2015/V115N8A6>
17. Kleynhans ELJ, Beukes JP, Van Zyl PG, Kestens PHI, Langa JM (2012) Unique challenges of clay binders in a pelletised chromite pre-reduction process. Miner Eng 34:55–62. <https://doi.org/10.1016/j.mineng.2012.03.021>
18. Riekkola-Vanhanen M (1999) Finnish expert report on best available techniques in ferrochromium production. Technical report Finnish Environment Institute
19. Beukes JP, Dawson NF, Van Zyl PG (2010) Theoretical and practical aspects of CR(VI) in the south african ferrochrome industry. Proc 12th Int Ferroalloys Congr. 53–62
20. Bale CW, Chartrand P, Degterov SA, Eriksson G, Hack K, Ben Mahfoud R, Melançon J, Pelton AD, Petersen S (2002) FactSage thermochemical software and databases. Calphad 26:189–228. [https://doi.org/10.1016/S0364-5916\(02\)00035-4](https://doi.org/10.1016/S0364-5916(02)00035-4)
21. Itaka K, Ogasawara T, Boucetta A, Benioub R, Sumiya M, Hashimoto T, Koinuma H, Furuya Y (2015) Direct carbothermic silica reduction from purified silica to solar-grade silicon. J Phys Conf Ser 596:12015–12015. <https://doi.org/10.1088/1742-6596/596/1/012015>